Integrated Aerodynamic and Structural Blade Shape Optimization of Axial Turbines Operating With Supercritical Carbon Dioxide Blended With Dopants

Abdelrahman S. Abdeldayem[1]
Thermo-Fluids Research Centre,
School of Science & Technology, City,
University of London,
London EC1V 0HB, UK
e-mail: abdel-rahman.abdeldayem@city.ac.uk

Martin T. White
Thermo-Fluids Research Centre,
School of Science & Technology, City,
University of London, London EC1V 0HB, UK

Andrea Paggini
Turbomachinery & Process Solutions,
Baker Hughes,
Via Felice Matteucci,
Firenze 50127, Italy

Marco Ruggiero
Turbomachinery & Process Solutions,
Baker Hughes,
Via Felice Matteucci,
Firenze 50127, Italy

Abdulnaser I. Sayma
Thermo-Fluids Research Centre,
School of Science & Technology, City,
University of London,
London EC1V 0HB, UK

Within this study, the blade shape of a large-scale axial turbine operating with sCO_2 blended with dopants is optimized using an integrated aerodynamic-structural three-dimensional (3D) numerical model, whereby the optimization aims at maximizing the aerodynamic efficiency whilst meeting a set of stress constraints to ensure safe operation. Specifically, three candidate mixtures are considered, namely, CO_2 blended with titanium tetrachloride ($TiCl_4$), hexafluorobenzene (C_6F_6), or sulfur dioxide (SO_2), where the selected blends and boundary conditions are defined by the EU project, SCARABEUS. A single passage axial turbine numerical model is setup and applied to the first stage of a large-scale multistage axial turbine design. The aerodynamic performance is simulated using a 3D steady-state viscous computational fluid dynamic (CFD) model while the blade stress distribution is obtained from a static structural finite element analysis simulation (FEA). A genetic algorithm is used to optimize parameters defining the blade angle and thickness distributions along the chord line while a surrogate model is used to provide fast and reliable model predictions during optimization using a genetic aggregation response surface. The uncertainty of the surrogate model, represented by the difference between the surrogate model results and the CFD/FEA model results, is evaluated using a set of verification points and is found to be less than 0.3% for aerodynamic efficiency and 1% for both the mass-flow rate and the maximum equivalent stresses. The comparison between the final optimized blade cross section has shown some common trends in optimizing the blade design by decreasing the stator and rotor trailing edge thickness, increasing the stator thickness near the trailing edge, and decreasing the rotor thickness near the trailing edge and decreasing the rotor outlet angle. Further investigations of the loss breakdown of the optimized and reference blade designs are presented to highlight the role of the optimization process in reducing aerodynamic losses. It has been noted that the performance improvement achieved through shape optimization is mainly due to decreasing the endwall losses with both the stator and rotor passages.
[DOI: 10.1115/1.4055232]

Keywords: axial turbines, blade-shape optimization, supercritical carbon dioxide, sCO_2, sCO_2 blends

1 Introduction

Introducing new working fluids like supercritical carbon dioxide (sCO_2) and sCO_2 blended with dopants in power generation cycles has a high potential to increase thermal efficiency and decrease the associated capital and operational costs [1,2]. Numerous studies have focused on analyzing the performance of pure sCO_2 power plants as well as sCO_2 mixtures [3] where the results have proven that introducing blends to the cycle potentially increases the efficiency and ensures feasible operation of transcritical power cycles, especially in hot weather. As part of the EU project, SCARABEUS, three candidate blends, namely, titanium tetrachloride ($TiCl_4$), hexafluorobenzene (C_6F_6), and sulfur dioxide (SO_2), have been proposed to raise the critical temperature of the mixture beyond that of pure CO_2 and allow condensation in transcritical power cycles. Crespi et al. [4] investigated the power cycle thermal efficiency gain by blending carbon dioxide with C_6F_6 and $TiCl_4$. The results of cycle analyses have shown that sCO_2 blends, with blend molar fractions of 10–25%, have thermal efficiency gains of 4–5 percentage points over the pure sCO_2 cycle due to the deleterious effect of high ambient temperatures on the compression process in the latter cycles. The use of CO_2 blended with SO_2 has also been considered through an economic and thermodynamic assessment which revealed an increase in cycle thermal efficiency of 2.33% relative to the pure sCO_2 cycle and a reduction of the power block capital expenses of 160 $/kW$_{el}$ for a 100 MW_{el} power cycle [5].

The turbomachinery components operating with sCO_2 and sCO_2 mixtures have been previously introduced [6,7]. The performance of different blends and the effect of blend fraction have also been investigated [8] with much focus on predicting the thermodynamic properties of mixtures, including the selection of equation of state and the optimum binary interaction parameters [9].

The design process of turbines operating with sCO_2 mixtures introduces some technical challenges related to the availability of

[1]Corresponding author.

Manuscript received July 10, 2022; final manuscript received July 17, 2022; published online September 12, 2022. Editor: Jerzy T. Sawicki.

loss models used for preliminary design. Specifically, the available performance estimation tools and correlations are calibrated for traditional working fluids like steam and air, whilst novel methodologies are required to simulate newly developed working fluids [10]. The design process of a turbine first requires a mean-line flow path design, from which a one-dimensional geometry is generated that can be used as the base to create the three-dimensional (3D) blade and run computational fluid dynamics (CFD) simulations. Blade shape optimization is then one of the promising techniques to optimize the turbine design by refining the flow path geometry to obtain the highest possible aerodynamic performance while maintaining certain structural limits to ensure a safe and reliable design.

Blade shape optimization has been widely investigated throughout the literature using different approaches, tools, and methodologies. Sathish et al. [11] conducted the blade shape optimization of a 10 MW sCO_2 axial turbine stage aiming at minimizing the blade profile losses while maintaining certain limits to the geometry. The selected geometric modeling platform was CAESES while the numerical flow solver was MISES. Many authors have used the commercial flow solver ANSYS CFX to simulate the aerodynamic performance in their optimization models [12–16] while the optimization solver is commonly a genetic algorithm or a multi-objective genetic algorithm [17–19]. Various optimization objectives have been presented through the published studies, however, the common target is achieving higher aerodynamic performance. Berchiolli et al. [13], Klonowicz et al. [14], Asgarshamsi et al. [17], and Kawatsu et al. [19] have defined the optimization objectives explicitly to maximize the overall turbine efficiency while Cho et al. [20] and Ennil et al. [16] have minimized the total pressure loss coefficient.

Decision variables selected for the blade shape optimization models are usually linked to geometrical parameters defining the airfoil shape in two-dimensional models [18] and 3D angles in 3D models [14]. The geometrical representation of the blade is critical to defining the number of decision variables that need to be included. Ennil et al. [16] introduced 11 parameters including flow angles, axial blade chord, turning angle, leading-edge radius, and trailing edge thickness to represent the airfoil shape of the blade. A similar approach is followed by Ref. [20], in which the authors defined the blade using 13 parameters. In more sophisticated studies, a larger number of variables are used to parametrize the pressure and suction sides of the blade using control point coordinates. Berchiolli et al. [13] introduced 48 decision variables and Klonowicz et al. [14] introduced 50 decision variables in their model including 3D aspects such as rotor blade twist angle, circumferential lean, and axial sweep angles. In some specific applications, decision variables are limited to certain parameters that define a part of the blade to minimize a specific source of loss; e.g., optimizing the blade tip to minimize tip leakage characteristics [12].

Due to the large number of decision variables required to represent a complete blade shape, a common optimization approach is based on replacing the physical CFD model with a surrogate model to give faster response during the optimization process. Surrogate models are created using a number of physical CFD simulations while the model response is extended by creating a relation between inputs and outputs using machine learning techniques. A set of case studies are first designed using a design of experiments algorithm (DoE) that creates a map of trial cases from which a relation between the inputs and outputs can be constructed. The response surface is then created using one of the various techniques including Kriging [19], artificial neural network [12,21], extreme learning machine, and support vector machine [12].

The optimization constraints are introduced to the model to verify the feasibility of the different candidate designs generated using combinations of decision variables. Berchiolli et al. [13] constrained the power output, the global maximum Mach number, and the stator and rotor factor of safety while other studies were only concerned with geometric constraints to ensure that the optimized profile meets all engineering constraints [11,20]. The structural analysis is important to ensure a safe blade design and has been introduced in many studies [22,23], although with added complexity to the model. Common materials in structural simulations of axial turbines are Inconel 718 [22], Inconel 738 [13] and 12% Chromium steel [11]. The loading in structural analysis is defined using either mechanical loading due to aerodynamic pressure distribution [22] or thermal loading due to temperature distribution, especially for cooled blades [23].

The performance of the reference and optimized blades can be further investigated by obtaining the loss breakdown structure using one of the loss audit techniques published in the literature [24–26]. The loss audit helps to highlight the dominant sources of aerodynamic losses so that the most significant improvements are revealed. Common types of aerodynamic losses in a subsonic axial turbine stage operating under design conditions are endwall, profile, trailing edge, and tip clearance losses.

In this paper, three working fluids have been considered for the design of a large-scale multistage axial flow turbine, namely, CO_2 blended with $TiCl_4$, hexafluorobenzene (C_6F_6), or sulfur dioxide (SO_2). The design process is based on numerical simulations rather than using existing mean-line design correlations since the latter are not calibrated for these working fluids. The design is further refined using a blade shape optimization model that aims at maximizing the performance of the turbine given certain structural constraints. A comparison between the reference and optimized blade profiles is presented and discussed to reveal different design aspects associated with different sCO_2 blends. The loss breakdown is illustrated for different working fluids compared to the reference design to show the link between turbine efficiency and different sources of aerodynamic loss.

2 Numerical Model

The blade shape optimization process is reported in Fig. 1 and is constructed from a numerical model composed of an aerodynamic solver (CFD), a mechanical solver (finite element analysis (FEA)), a design of experiments (DoE) algorithm, a surrogate model, and an optimization solver. The baseline blade geometry is created using a mean-line design model [27] that is developed for the SCARABEUS project [28] to design a large-scale blended sCO_2 turbine using the Aungier [29] loss model. Geometrical parameters including the number of stages, hub diameter, blade height, blade inlet/outlet angles, stagger angle, chord length, number of blades, and trailing edge (TE) thickness are used to create the 3D blade along with assumptions defining the inlet/outlet wedge angles, leading-edge thickness, and control points defining thickness distribution of the airfoil. In order to assess the blades stresses, simplified shroud and hub geometries are used for the stator and rotor blade geometries, respectively, whereby a fillet is applied at the base of each blade to make the mechanical analysis more realistic. The results of aerodynamic solver are transferred back to the mechanical solver so that the pressure load on the blade surface can be evaluated. A set of design points are then created using the DoE algorithm and solved to create a response surface surrogate model which replaces the physical CFD/FEA model to simplify the optimization process and allow for more optimization runs in a reasonable time frame.

2.1 Computational Fluid Dynamic Model. To investigate and compare the effect of different sCO_2 blends on the blade shape design, and further investigate the performance of the optimized blades against the reference designs, a 3D steady-state CFD model of the first stage of each blend design is setup. Although the proposed turbine designs are multistage, the CFD model is setup for the first stage of each design to minimize the number of decision variables for the optimization and limit the computational power needed for this study to a reasonable time frame. Similar flow conditions defined by equal enthalpy drop per stage, equal rotational speed, and equal hub diameter are preserved for each case to ensure a fair comparison between the different

blends. To achieve that, the number of stages for each blend is adjusted to give almost the same enthalpy drop per stage, thus the velocity triangles of the first stage of the three turbines, according to the mean-line calculations, are identical.

The operating conditions for the proposed case studies are part of the work conducted within the SCARABEUS project [28] where the cycle analysis generates the boundary conditions at the turbine inlet and outlet as well as the optimum blend molar fraction. The model definition of each turbine is further investigated using a mean-line design tool developed based on the Aungier loss model [29] to generate a preliminary design of the turbines. The model definition of the proposed blends is presented in Table 1. The model uses shear stress transport (k–ω SST) turbulence model as it has been found that this is the most suitable model for turbomachinery applications [30]. The interface between the stator and rotor domains is treated as a mixing plane which has proven to give high-quality results with the least numerical instabilities compared to the frozen rotor approach [31]. The rotor layout is considered to be unshrouded with a tip clearance of 0.07% of the tip diameter for each case.

The mesh quality has been controlled by adjusting the mesh size near the walls while maintaining $y^+ \approx 50$ where standard wall functions are best suited [32]. The number of grid points within the rest of the domain is obtained as the minimum number of grid points required for a mesh independent solution. The convergence criteria of the mesh study have been selected as the total-to-total efficiency (η_{tt}) where the tolerance is set to 0.5% compared to the finest mesh. The mesh independence study results are presented in Fig. 2 for the sCO_2–C_6F_6 case study as a sample case, where the number of grid points reported is the summation of stator and rotor domains.

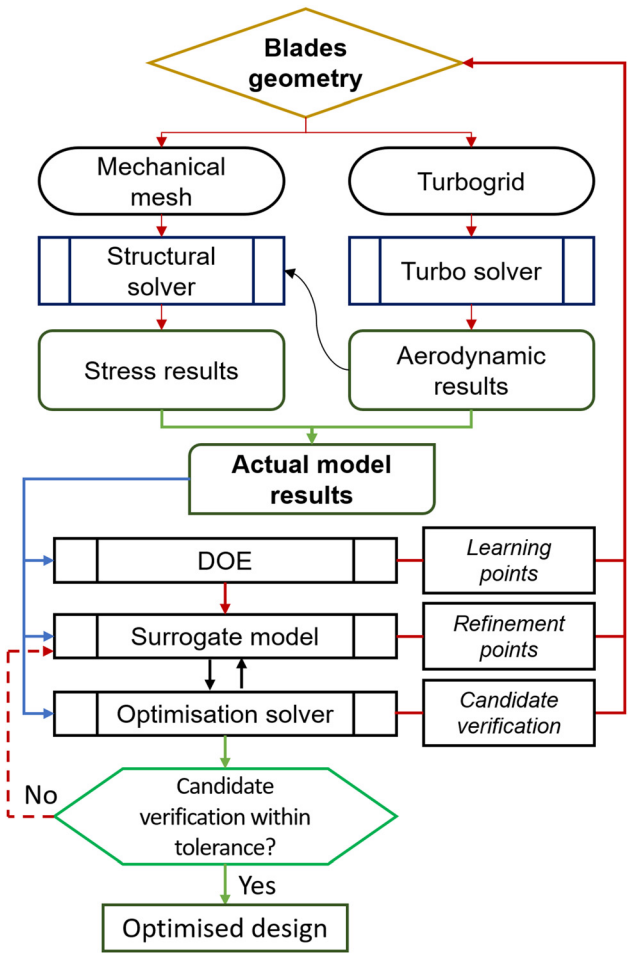

Fig. 1 Overview of the optimization model

The thermophysical properties of the sCO_2 mixtures are evaluated using the "SIMULIS" software package. The selected equation of state is PengRobinson, and the binary interaction parameters for each blend are set according to a sensitivity study carried out by our project partners [5,9]. These parameters are the same as the values defined in the cycle analysis and mean-line design stages. However, it is worth noting that the mixture modeling is most critical when modeling the thermodynamic cycle, and there is not a large sensitivity when considering the turbine in isolation because the turbine operates quite far from the critical point of the fluid where non-ideal effects are most significant [9].

The properties are introduced to the CFD models using look-up tables that cover the expected pressure and temperature ranges with the size of 500×500 points. The selected pressure range is set to 10 and 300 bar since the turbine inlet total pressures are 250 bar and the outlet static pressure varies between 56 and 97 bar. This range covers any local regions with pressures higher than the inlet pressure or lower than the outlet pressures. Similarly, the temperature range is set between 400 and 1200 K. The CFD model results have been checked to ensure that the property tables can safely cover the global minimum and maximum properties where the table limits are found to be sufficiently far away from the obtained limits. Different sizes of the lookup tables have been tested ranging between 200×200 and 700×700 points while the variations in the model results are found to be negligible above 500×500.

2.2 Finite Element Analysis Model. The FEA model is setup using the same blade geometry defined for the CFD model. However, the blade geometry is modified by adding a solid base with a minimum thickness of 5 mm at the shroud of the stator and at the hub for the rotor with fillets applied between the blade and the supporting base to represent the physical turbine geometry after manufacturing. Adding the fillets also avoids numerically induced peak stresses, as indicated in Fig. 3.

The mesh in this model is setup with a large global element size to simplify the optimization process and reduce the overall model complexity while local refinement is applied at the base fillet where the peak stress point is expected to exist. With a growth rate of 1.1, which defines the ratio between the large elements at the tip and the small elements at the base, the overall mesh structure produces satisfactory results for a low number of elements. A mesh study is summarized in Fig. 4 where the different curves represent the global element size, and the callouts report the local element size at the base of the fillet in mm. It can be noted from the figure that decreasing the global mesh size affects the total number of nodes significantly while its effect on the stress values is negligible. However, the local mesh size has a large impact on the peak stresses. For that reason, a large global size of 3 mm is selected along with a local mesh size of 0.3 mm to achieve results of satisfactory quality with a low number of nodes. The stress results in this case showed a deviation within 2% of the most accurate value where the number of elements is around 90,000 and 120,000 for the stator and rotor blades, respectively.

Table 1 Design conditions for the three CO_2 blends

Working fluid	–	sCO_2–SO_2	sCO_2–C_6F_6	sCO_2–$TiCl_4$
Blend molar fraction	%	30	14.5	17
Inlet total pressure	bar	238.9	238.9	242.6
Inlet total temperature	K	973.15	973.15	973.15
Turbine outlet static pressure	bar	68.3	59.1	95.5
Mass flow rate	kg/s	780.84	877.3	1241.2
Stage 1 outlet static pressure	bar	207.5	199.5	200.1
Stage actual enthalpy drop	kJ/kg	18.8	18.8	18.8
Hub radius	mm	420	420	420
Rotational speed	RPM	3000	3000	3000
Number of stages	—	9	8	5

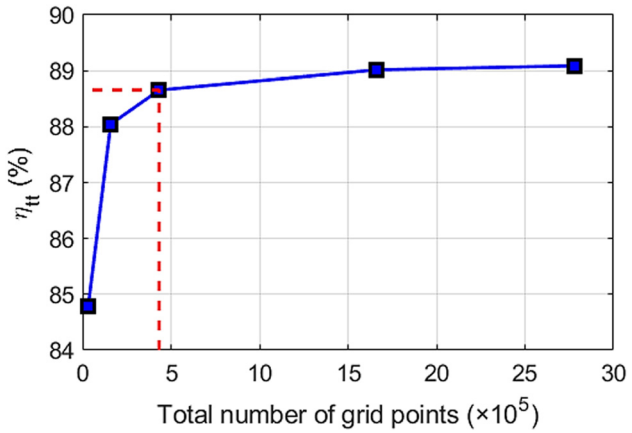

Fig. 2 Mesh independence study for the C_6F_6 case

The aerodynamic loads (i.e., pressure distribution over the blade surfaces) predicted within the CFD simulations are used as input boundary conditions for the FEA, along with the centrifugal load on the rotor blades due to rotation. The preliminary material selection process has considered Udimet 720, which is a nickel-based alloy commonly used with gas turbine blades that can operate at temperatures up to 1000 °C whilst maintaining a high yield strength and is suitable for the proposed operating conditions [33].

2.3 Surrogate Model. The surrogate model replaces the physical CFD/FEA model so that the objectives and constraints can be assessed rapidly. This can be achieved by building a relation between input geometrical parameters and output aerodynamic and structural performance parameters using machine learning techniques. In this study, the central composite design of the experiment algorithm is used to create a set of learning points according to a prespecified range for each input optimization variable [34]. In this method, the design points are selected to form the shape of a sphere with a center point in the middle surrounded by points on the axis and diagonal points; this process for two variables would create the shape in Fig. 5 [35].

The number of design points (N_{DP}) is linked to the number of input variables through the following equation:

$$N_{DP} = 1 + 2k + 2^{(k-f)} \tag{1}$$

where k is the number of input variables and f is a factor designed to limit the excessive increase in the number of design points for a large number of input variables. In Eq. (1), the first term is the center of the design points, the second term represents the points on the axis and the third term represents the diagonal points. The limiting factor is added to the diagonal points to decrease the number of diagonal points while maintaining the shape of the central composite design. The factor used by the solver (ANSYS workbench) for 11 input variables is 4 so the number of design points is 151. The disadvantage of this methodology is the uncertainty in the input/output relation. However, this can be assessed and improved using response surface verification and by defining additional refinement points, respectively.

Genetic aggregation response surface is selected for this study to develop the surrogate model as genetic aggregation response surface with autorefinement gives the best fit possible for each output parameter among the different types of response surface available (full second-order polynomial, non-parametric regression, Kriging, neural network, and sparse grid) [36]. Compared to the classical response of polynomial, non-parametric regression, or Kriging genetic aggregation, genetic aggregation takes more time because it solves the response surface for each output variable individually and the cross-validation process [37]. The initial number of learning points are generated using the design of experiments model while a set of refinement points are created to improve the accuracy of the response surface. The target uncertainty in total-to-total efficiency is selected to be ±0.1 pp and the maximum equivalent stress is ±5 MPa. The response surface results are verified against the results of the physical CFD/FEA model for a set of verification points to assess the uncertainty of the surrogate.

2.4 Optimization Model. To obtain the best blade shape, the optimization model is setup based on a set of geometrical parameters defining the blade shape while objectives and constraints are introduced to maintain efficient operation and a safe design. The blade geometry is represented by a uniform airfoil section along the blade radial direction because the blades are relatively short where the blade height to hub diameter is around 8%. The angle and thickness distributions along the chord line of the airfoil are defined from leading edge to trailing edge with four points on each curve, as reported in Fig. 6. The points are connected using a third-order polynomial rather than Bezier curves since polynomials give better control of the curvature with a lower number of points. As long as the axial location of the first and last points are fixed at the leading and trailing edge, respectively, the number of variables is six variables for each curve and 24 variables for the entire stage. However, based on trials assessing the sensitivity of the results to the number of decision variables, it has been found that achieving the desired uncertainty of the output parameters is not possible using reasonable computational power, and thus the surrogate model is unable to accurately represent the physical model. This is due to the large population size and the limited number of learning and refinement points. Moreover, it was found that solving more refinement points did not allow any significant improvement in the model's accuracy. Thus, to create a surrogate model within the acceptable output tolerance, a decision was made to reduce the number of decision variables. This was done by eliminating the less dominant variables.

The procedure followed to reduce the number of decision variables can be summarized in three steps. First, the streamwise division of the points is fixed for each curve so the x-values of the two midpoints are removed, such that each curve has four variables instead of six with a total number of variables of 16. Second, the inlet angle of the stator blade is considered fixed as the inlet flow velocity to the stage is always axial, which removes an additional variable. Finally, a preliminary sensitivity study has been conducted by creating a surrogate model using the 15 variables, as reported in Fig. 7. In this figure, Sa2 is the stator angle at point 2, Sa3 is the stator angle at point 3, Sa4 is the stator angle at point 4, St1 is the stator thickness at point 1, St2 is the stator thickness at point 2, St3 is the stator thickness at point 3, St4 is the stator thickness at point 4, Ra1 is the rotor angle at point 1, Ra2 is the rotor angle at point 2, Ra3 is the rotor angle at point 3, Ra4 is the rotor angle at point 4, Rt1 is the rotor thickness at point 1, Rt2 is the rotor thickness at point 2, Rt3 is the rotor thickness at point 3 and Rt4 is the rotor thickness at point 4. The points are labeled according to Fig. 6. The results reported in Fig. 7 show that the optimization is less sensitivite to the first and second thickness points for both rotor and stator blades, and hence these are omitted, and the total number of decision variables is reduced to 11.

The search space is defined by setting the upper and lower limits of each decision variable as summarized in Table 2. The upper and lower limits are selected around the reference values based on manual iterations that aimed at preserving a reasonable shape for the blade cross section.

The objective of this optimization run is to maximize the total-to-total efficiency, whilst targeting the mass-flow rate defined by the cycle analysis. The target mass-flow rates for the $TiCl_4$, C_6F_6, and SO_2 cases are 1241, 877, and 781 kg/s, respectively, while the target tolerance is set to ±2%. The structural constraints for both rotor and stator blades are set to not exceed a stress limit of 400 MPa, calculated by dividing the yield strength of the working

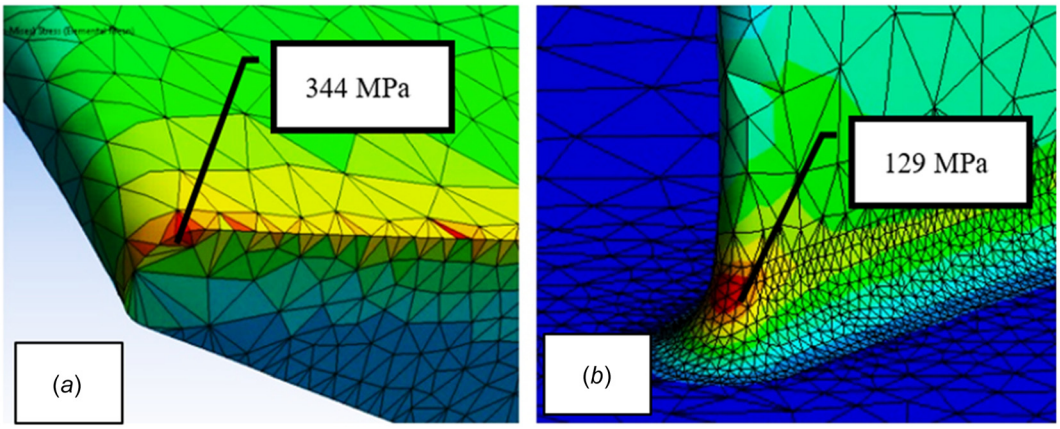

Fig. 3 Effect of base fillet on FEA results: (*a*) without fillet and (*b*) with fillet

material at 650 °C, which is around 1042 MPa [38], by a safety factor of 2.5.

The selected optimization solver is a genetic algorithm applied through ANSYS workbench and linked to the surrogate model. The initial population size and number of samples per iteration is 100. The convergence criteria are set to either achieve a stability percentage of 2% or reach a maximum number of iterations of 50. Once the optimization run is complete, five candidate points are calculated and verified against the physical model. The deviation between the physical model and response surface optimization results are then assessed to check the accuracy of the surrogate model. If the measured deviations are high, the response surface is further refined using the candidate points and the optimization process is repeated. Among the five candidate points, the design showing the best performance, as well as a good agreement with the verified results are selected.

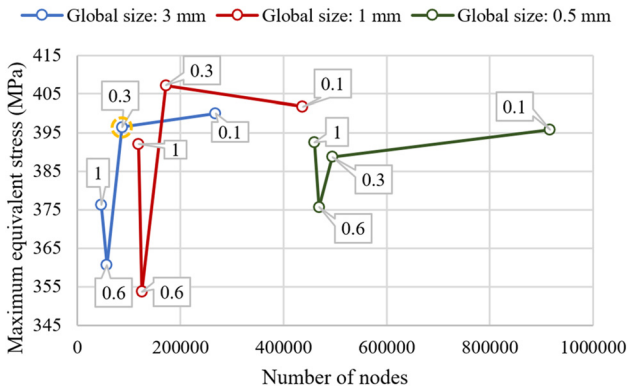

Fig. 4 FEA mesh analysis of the sCO_2–C_6F_6 stator blade for different global/local element sizes

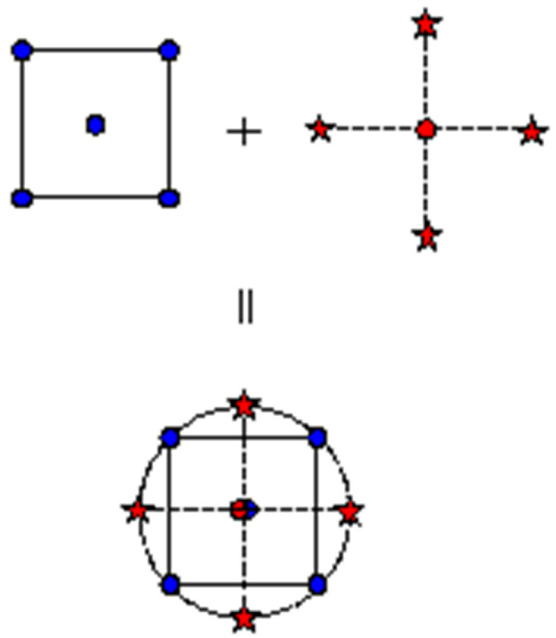

Fig. 5 Central composite design of two decision variables

3 Computational Fluid Dynamic/Finite Element Analysis Model Verification

Due to the fact that supercritical carbon dioxide is a recent technology and the experimental work in the literature is limited to small-scale radial turbomachines there is no suitable experimental data against which to validate the current CFD/FEA model for sCO_2 applications. However, the aerodynamic and structural

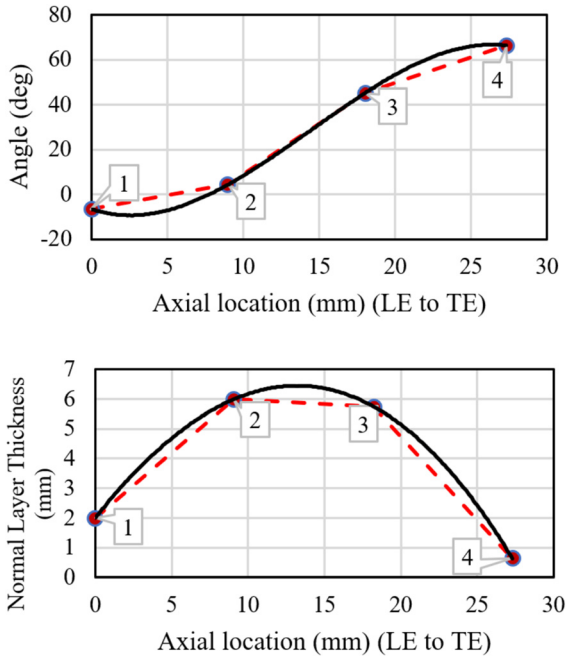

Fig. 6 Blade profile representation using angle and thickness distribution

solvers used in this study have been widely deployed in the analysis of other large-scale turbines, for example, Refs. [31] and [32]. A numerical model analyzing the conjugate aerodynamic-structural interaction of a 15 MW sCO_2 single-stage axial turbine is selected to verify the physical CFD/FEA model presented in this paper [7]. The case definition and the operating conditions are presented in Table 3.

A comparison of the main performance metrics as well as the structural simulation is summarized in Table 4. A good agreement is observed between the two models in terms of mass-flow rate, total-to-static efficiency, and maximum von mises stress with deviations of 4.5%, 0.2%, and 1.7%, respectively. However, larger deviations are observed for the power output and degree of reaction. This could be the result of an inaccurate replication of the geometry due to uncertainties in extracting precise shape data from published figures rather than explicit tables; although, the main geometric parameters like hub/shroud diameters, inlet/outlet blade angles, inlet/outlet fillet radii, stagger angle, and chord size are identical.

4 Results and Discussion

The blade shape of the first stage of a turbine designed for each of the three proposed working fluids is optimized and compared to the reference geometry obtained using a preliminary mean-line design tool. The performance of the optimized blades is further investigated by calculating the loss breakdown structure and comparing the results to the reference geometries to realize how the optimization process has controlled the performance and enhanced the total-to-total efficiency. The computer used to run these cases contains a 3 GHz processor with 36 cores, 48 MB cash memory, 128 GB of RAM and 2 TB solid state drive hard drive.

4.1 Optimized Blades Using Different Blends. Numerous design points are created using the high fidelity CFD/FEA model to create a response surface where 151 model are created using the design of experiments algorithm and an additional 250 design points are created by the response surface solver as refinement points to improve the accuracy of the surrogate model. For each design point, 11 geometric parameters are defined as inputs while the main objectives and constraints are evaluated to form the learning points of the surrogate model. Verification points are introduced to evaluate the performance of the surrogate model and its uncertainty. The uncertainty of the optimized candidate design points is found to be less than 0.3% for the total-to-total efficiency and 1% for the mass-flow rate, stator maximum stress, and rotor maximum stress in all the proposed cases.

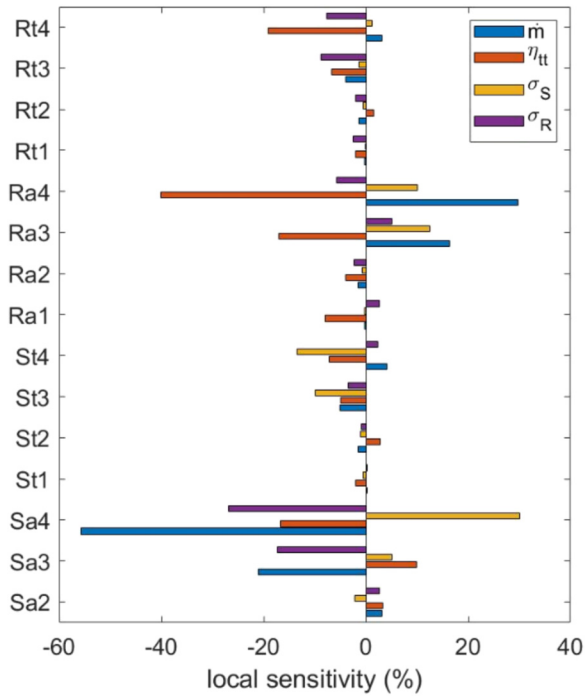

Fig. 7 Preliminary sensitivity study solving 15 decision variables, sCO_2–SO_2 model

Table 2 Decision variables

Parameter	Unit	Value		
		Reference	Minimum	Maximum
St3	mm	5.7	4	7
St4	mm	0.7	0.2	1
Sa2	deg	5	–5	15
Sa3	deg	45	35	55
Sa4	deg	66.3	55	80
Rt3	mm	5.6	4	7
Rt4	mm	0.7	0.2	1
Ra1	deg	0	–10	10
Ra2	deg	–5	–15	5
Ra3	deg	–45	–55	–35
Ra4	deg	–64.93	–75	–55

The response for different working fluids following the prespecified ranges of decision variables are evaluated and the results ranges are recorded in Table 5 where, η_{tt} is the total-to-total efficiency percentage, $\dot{m}$ is the mass-flow rate in kg/s, σ_S is the stator maximum equivalent stress in MPa and σ_R is the rotor maximum equivalent stress in MPa. These results include the size of the search space covered within this study. It can be noted that changes to the blade profile can lead to significant deviations in key parameters like mass-flow rate and stress levels, as well as the total-to-total efficiency. The sensitivity of the output parameters to the inputs is evaluated and further discussed in Sec. 4.4, which can inform the elimination of less important input variables to reduce computational power and decrease the uncertainty of the surrogate model. This can be expected to speed up the design process when the optimization is applied to all the stages of the final SCARABEUS turbine.

The optimized blades for different sCO_2 blends are introduced in Fig. 8 and compared to the reference geometries for both the rotor and stator blades. The optimized blade geometry of the first stage of the sCO_2–SO_2 case study is shown in Fig. 8(*a*) where it can be seen that the stator blade curvature is relaxed near the trailing edge to decrease the stator outlet angle. Subsequently, the rotor leading edge angle is decreased in response to the changes made to the stator, and decreased near the trailing edge, while the trailing edge thickness is decreased by almost 60% to decrease trailing edge losses. These changes improve the aerodynamic performance by decreasing the deviation angle between the flow stream and the blade.

By investigating the optimized blade geometry of the sCO_2–C_6F_6 case study (Fig. 8(*b*)), similar trends to the SO_2 blades are observed where the stator angle distribution near the trailing edge is decreased while the thickness of the stator blade near the trailing edge is increased. The rotor thickness is decreased near

Table 3 Definition of the verification case study

Parameter	Unit	Value
Turbine inlet pressure	bar	130
Turbine inlet temperature	K	773
Turbine outlet pressure	bar	80
Mean blade diameter	mm	389
Rotational speed	RPM	10,000
Mass flow rate	kg/s	250

Table 4 Results of the verification case study

Parameter	Unit	Reference [7]	Numerical model	Deviation (%)
Mass flow rate	kg/s	250	238.81	–4.5%
Power	MW	15	13.75	–8.3%
Degree of reaction	—	0.28	0.3	7.1%
Flow coefficient	—	0.55	0.569	3.5%
Total to static efficiency	%	83.96	83.782	–0.2%
Rotor maximum deflection	mm	0.061	0.056	–8.2%
Rotor maximum Von Mises stress	MPa	646.8	636	–1.7%

Table 5 Calculated ranges of output parameters

	SO_2		C_6F_6		$TiCl_4$	
	Minimum	Maximum	Minimum	Maximum	Minimum	Maximum
η_{tt}	69.8	93.9	60.5	93.7	76.5	94.8
$\dot{m}$	270.1	1449.6	385	1520	238	2182
σ_S	60	1380	90	827	69.6	3608
σ_R	45.2	490	57	563	36	728

the second half of the blade and at the trailing edge while the angle distribution along the rotor chord line has been slightly modified by decreasing the blade angle within the first half of the airfoil and increasing the blade angle within the second half. The optimized blade geometry of the sCO_2–$TiCl_4$ case study (Fig. 8(*c*)) shows similar trends to the other two blends in decreasing the rotor outlet angle and decreasing the trailing edge thickness of both rotor and stator; however, the blade angle within the first part of the rotor is significantly decreased.

A comparison of the reference and optimized blade thickness and angle distributions is provided for each blend in Fig. 9. The results correspond to the changes reported in Fig. 8 and provide the optimized distributions explicitly. The performance improvement for the three proposed working fluids is reported in Table 6. It could be seen from the table that the optimization has succeeded in increasing the total-to-total efficiency for the three blends, whilst achieving a design with a feasible mass-flow rate, as prescribed by the cycle requirements, and that ensures safe operation with a peak equivalent stress less than 400 MPa. It should be noted that the reference values mentioned in the table are calculated using the physical model, and report some deviations compared to the mean-line design model. Some deviations between the mean-line design and CFD model results are expected due to the inherent simplicity of the mean-line approach, and the limitations of the mean-line model in evaluating aerodynamic losses by using loss correlations developed for traditional working fluids. However, these have been investigated and quantified by the authors [30]. Absolute efficiency increase of 2.54 pp, 2.06 pp, and 1.76 pp is achieved for the sCO_2–SO_2, sCO_2–C_6F_6, and sCO_2–$TiCl_4$ designs, respectively. By comparing achieved efficiencies for the different blends, it can be seen that the highest efficiency is obtained for the $TiCl_4$ design which is 0.12 pp larger than the C_6F_6 design and 0.13 pp larger than the SO_2 design, while the efficiencies obtained for the C_6F_6 and SO_2 designs are almost the same.

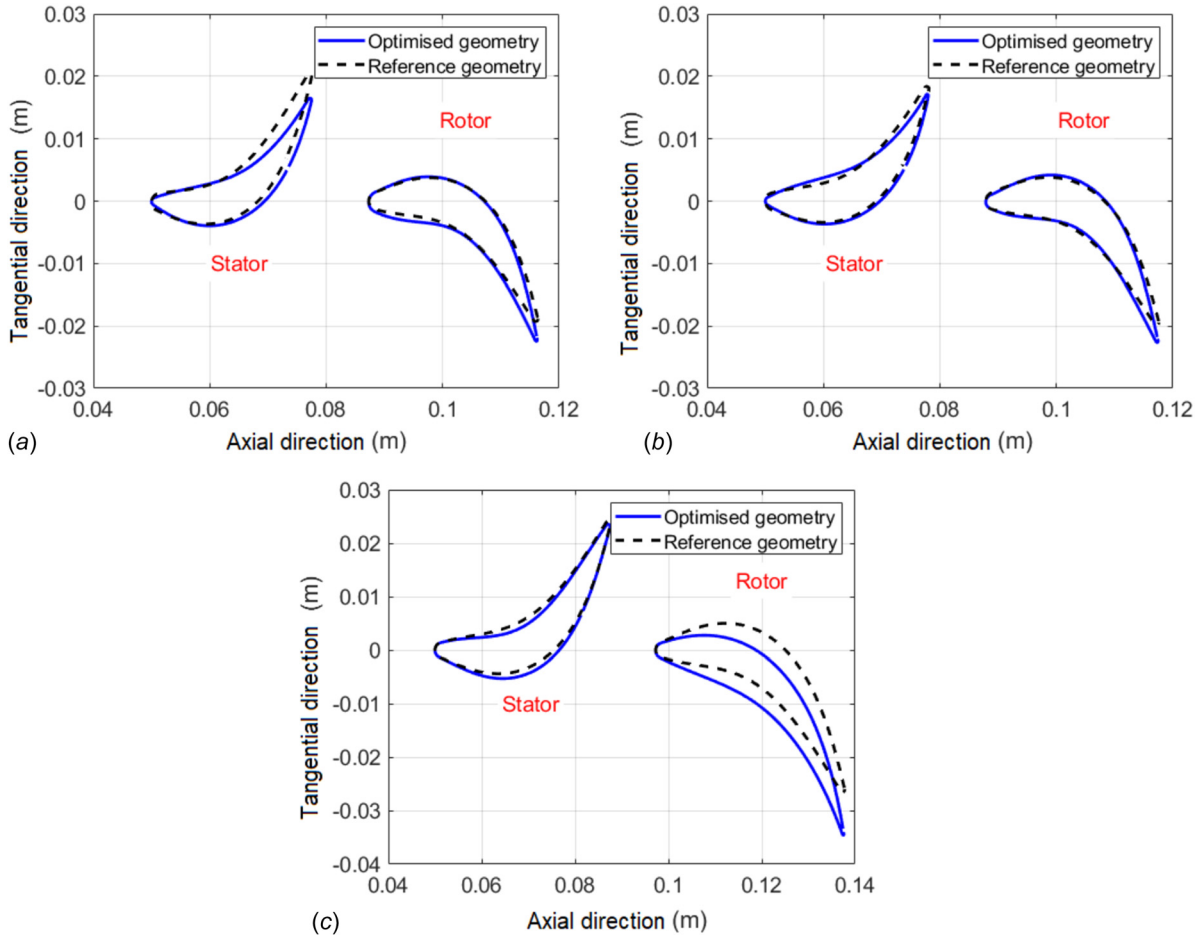

Fig. 8 Comparison between reference and optimized blades of the first stage for (*a*) sCO_2–SO_2, (*b*) sCO_2–C_6F_6, and (*c*) sCO_2–$TiCl_4$

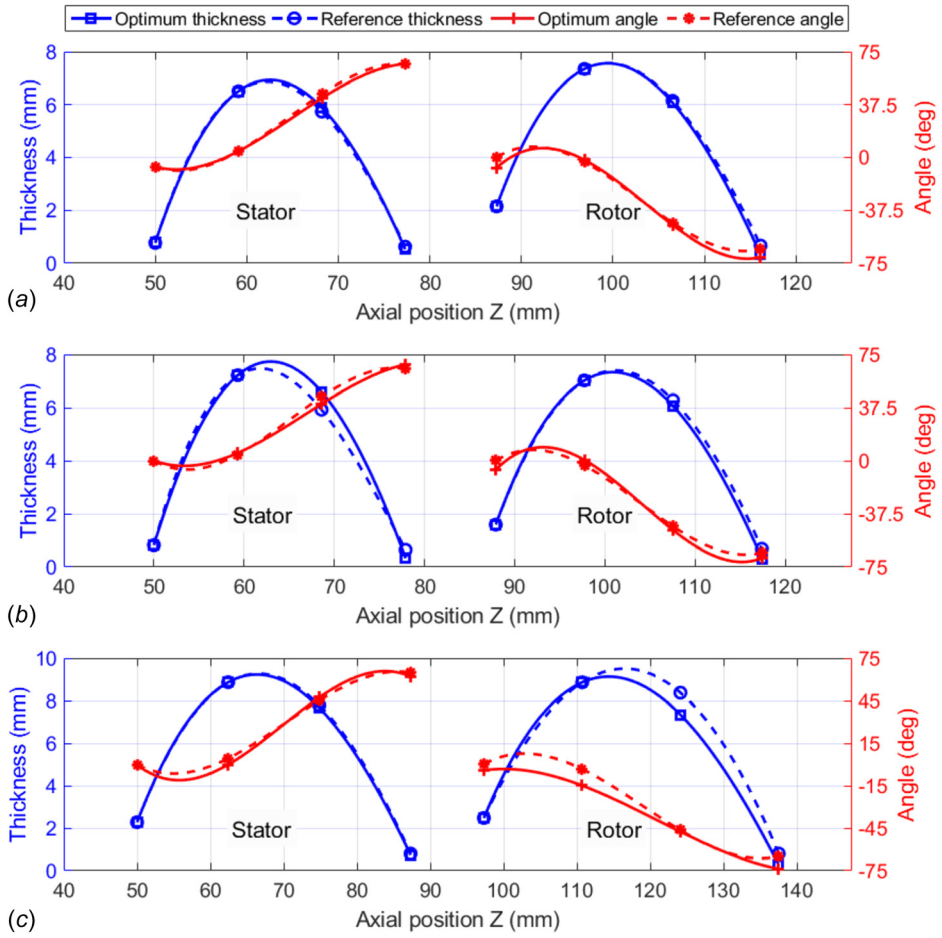

Fig. 9 Comparison between reference and optimized blade thickness/angle distribution for different blends: (*a*) sCO_2–SO_2, (*b*) sCO_2–C_6F_6, and (*c*) sCO_2–$TiCl_4$

The mass-flow rate decreased in all the designs to bring the design within the feasible range of operation defined by ±2% of the target mass-flow rate defined in Table 1 because the mean-line design has been found to underestimate the mass-flow rate at the reference design point. The reduction in mass-flow rate is reflected by a reduction in power output although the efficiency is increased. The results in Table 6 show that the best performance is obtained for the three blends at a slightly larger degree of reaction, typically around 0.63, compared to the value of 0.5 assumed during the preliminary calculations. The flow coefficient is very close to the preliminary design value of 0.5 and the loading coefficient is around 10% larger than the preliminary design value. For the stress limits, the reference design points of the SO_2 stator and the $TiCl_4$ stator are unsafe with maximum stress values over the limit of 400 MPa; however, the optimized design points succeed at maintaining peak stresses under the limits for all the design case studies.

To further understand the differences between the blade shapes of the three blends, the optimized airfoils are reported in Fig. 10. It is expected that the differences between the three cases are not only due to the differences in properties, but also due to the different boundary conditions generated from the thermodynamic cycle optimization for each three blends. Thus, the influence of these effects on the resulting blade shape and aerodynamic performance is combined and they cannot be easily separated. However, the larger chord size of the $TiCl_4$ case can be clearly noted, which results from the higher stresses that are estimated during the preliminary mean-line design phase which drives the design to a lower number of blades per stage. Subsequently, the pitch and chord size are both increased to maintain a fixed pitch to chord ratio. The similarity between SO_2 and C_6F_6 designs reflects the similarity of the properties of the mixtures, the cycle layout, and the boundary conditions reported in Table 1. The blade shape differences can also be linked to the mixtures properties by comparing the hydraulic properties of the three mixtures reported in Table 7. It can also be seen that the blade thickness is higher near the leading edge for the $TiCl_4$ case, followed by C_6F_6 and SO_2, reflecting the density variations as the higher the density, the

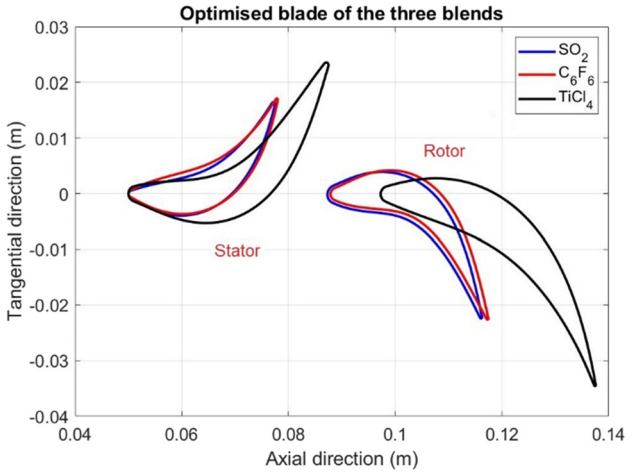

Fig. 10 Comparison between optimized blade shapes for the three blends

Table 6 Results of optimizing blade shapes

Parameter	Unit	SO_2 reference	SO_2 optimum	C_6F_6 reference	C_6F_6 optimum	$TiCl_4$ reference	$TiCl_4$ optimum
Total-to-total efficiency	%	88.82	91.36	89.31	91.37	89.69	91.45
Mass flow rate	kg/s	814.4	790.65	989.4	879.1	1426.3	1252.5
Power	MW	15.05	14.69	18.24	16.59	25.35	23.54
Degree of reaction	—	0.32	0.65	0.44	0.62	0.45	0.62
Flow coefficient	—	0.51	0.53	0.56	0.51	0.56	0.53
Loading coefficient	—	0.89	1.12	0.91	1.09	0.86	1.14
Stator maximum stress	MPa	447.42	347.42	393.30	346.55	509.12	401.44
Rotor maximum stress	MPa	188.76	246.67	210.98	244.00	250.67	392.06

lower the flow path cross section and the thicker the blade. The difference between inlet and outlet blade angles reflects the variation in the dynamic viscosity to reduce secondary flows, where the higher the viscosity the lower the difference in the blade angles. This is clear from Fig. 10, as the highest blade angle variation appears in the SO_2 case, followed by the C_6F_6 and $TiCl_4$ cases.

4.2 Loss Breakdown Analysis. The performance of the proposed designs is further investigated by analyzing the aerodynamic loss structure of the reference and optimized geometries to compare the weight of different sources of loss. The expected aerodynamic losses of a subsonic axial turbine stage running at the design operating conditions are the endwall losses, profile losses, trailing edge losses and tip clearance losses [39]. An overview of the loss structure is shown in Fig. 11 where the entropy distribution along the axial direction from inlet to outlet is presented. The stator domain is represented along the axial direction from 0 to 1, while the rotor domain is represented between 1 and 2. The calculated entropy values are massflow averaged quantities evaluated at different axial locations along the streamwise direction. The dominating loss regions can be directly identified from the figure given the axial locations of the stator/rotor blades, inlet/outlet domains, and the stator/rotor axial gap.

The reference cases lead to a larger entropy increase at the stage outlet in all the designs reflecting the achieved performance improvement by optimizing the blade geometries for the three proposed blends. The curves for the SO_2 and C_6F_6 designs are close to each other while the $TiCl_4$ design reports less entropy generation with a higher total-to-total efficiency. This is in agreement with the efficiency results mentioned in Table 6. A significant reduction in entropy generation in both the rotor and stator blades can be observed in the figure and can be further clarified by carrying out a loss audit of the reference and optimized designs.

The loss breakdown is obtained following the approach described by De Servi et al. [25] where the sources of loss are evaluated by setting up three CFD models for each design point according to the structure mentioned in Table 8. The difference between the entropy generation from model one and two accounts for the tip leakage loss while the total entropy rise in the second model is due to end wall, profile, and trailing edge losses in the rotor and stator. To quantify each source individually, the third model eliminates end wall effects by setting free slip boundary conditions near the end walls so that the remaining losses are profile and trailing edge losses. The difference between entropy from inlet to a plane at the trailing edge accounts for the profile losses while the difference between the plane at the trailing edge and the outlet plane is due to the trailing edge losses. By subtracting the values obtained from model two and model three, endwall losses can be evaluated.

A complete loss breakdown structure of the reference and optimized blades for the three blends are summarized in Fig. 12 where the losses due to stator endwall, stator profile, stator trailing edge (STE), rotor endwall, rotor profile, rotor trailing edge (RTE), and tip clearance are presented. The reference points show a high entropy increase relative to the optimized blades for all the

Table 7 Properties of the three mixtures at the inlet conditions

	SO_2	C_6F_6	$TiCl_4$
Molar fraction (%)	30	14.5	17
Density (ρ) (kg/m^3)	146.6	185.4	200.5
Dynamic viscosity (μ) (Pa · s)	4.70×10^{-5}	5.05×10^{-5}	5.11×10^{-5}

Table 8 Loss breakdown approach by De Servi et al.

Model	Description
Model 1: standard model	Total entropy increase (inlet to outlet)
Model 2: no tip clearance	Entropy increase across stator and rotor individually from inlet to outlet
Model 3: no tip clearance/endwall	Entropy increases from inlet to location at the trailing edge and from trailing edge to an outlet for stator and rotor blades

working fluids with the highest value for the SO_2 design followed by C_6F_6 and the $TiCl_4$, respectively. By looking at the SO_2 design it could be seen that both stator and rotor loss components are reduced with a dominant reduction in the stator endwall, stator trailing edge, and rotor endwall losses. Similar findings are recorded for the C_6F_6 design, however, the reduction in the tip clearance is substantial. For the $TiCl_4$ design, tip clearance losses are increased, but with a reduction to stator endwall, stator profile, stator trailing edge, rotor endwall, and rotor trailing edge losses.

The differences between reference and optimized loss breakdown components for the three blends have shown that the blade profile generated using the mean-line design is not ideal and

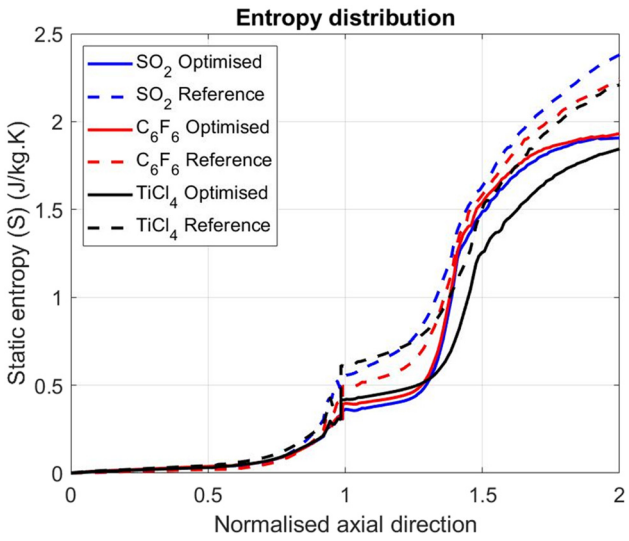

Fig. 11 Entropy distribution along the normalized axial direction for the first stage from inlet to outlet for different blends

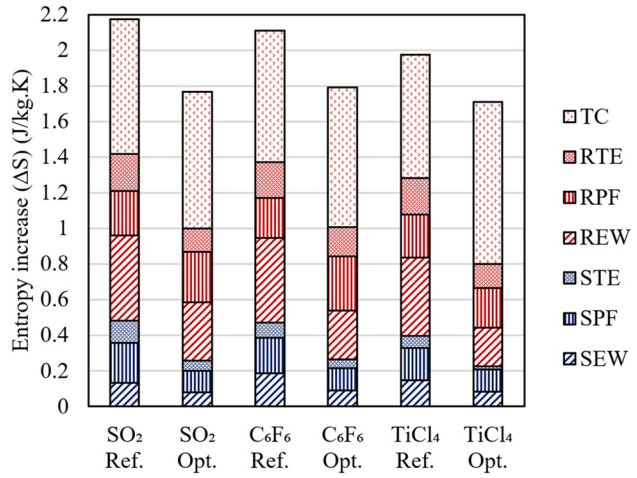

Fig. 12 Loss breakdown structure for reference and optimized geometries

generates large secondary flows and vortices compared to the optimized profiles as noted from the reduction in secondary flows and profile losses. The trailing edge losses also show a reduction in both the stator and rotor blades indicating an over estimation of trailing edge blade thickness within the mean-line design model; however, trailing edge losses are not overly dominant. The tip clearance shows minor changes due to design optimization which means that it cannot be improved using profile modifications; this is expected as tip clearance losses are mainly due to the tip gap thickness and the stage pressure ratio [40].

The contribution of each source of loss to the total aerodynamic performance is summarized in Table 9 where it is observed that the largest portion is due to tip leakage and the smallest portion is due to trailing edge loss. The endwall and profile losses are similar in most of the designs, although the endwall losses are higher than the profile losses in the reference design point. However, the optimized designs show less endwall losses indicating that the endwall losses are more affected by the optimization process.

4.3 Sensitivity of Output Components. The number of decision variables needed to represent a single blade profile is relatively large, and this does not account for the blade shape radial

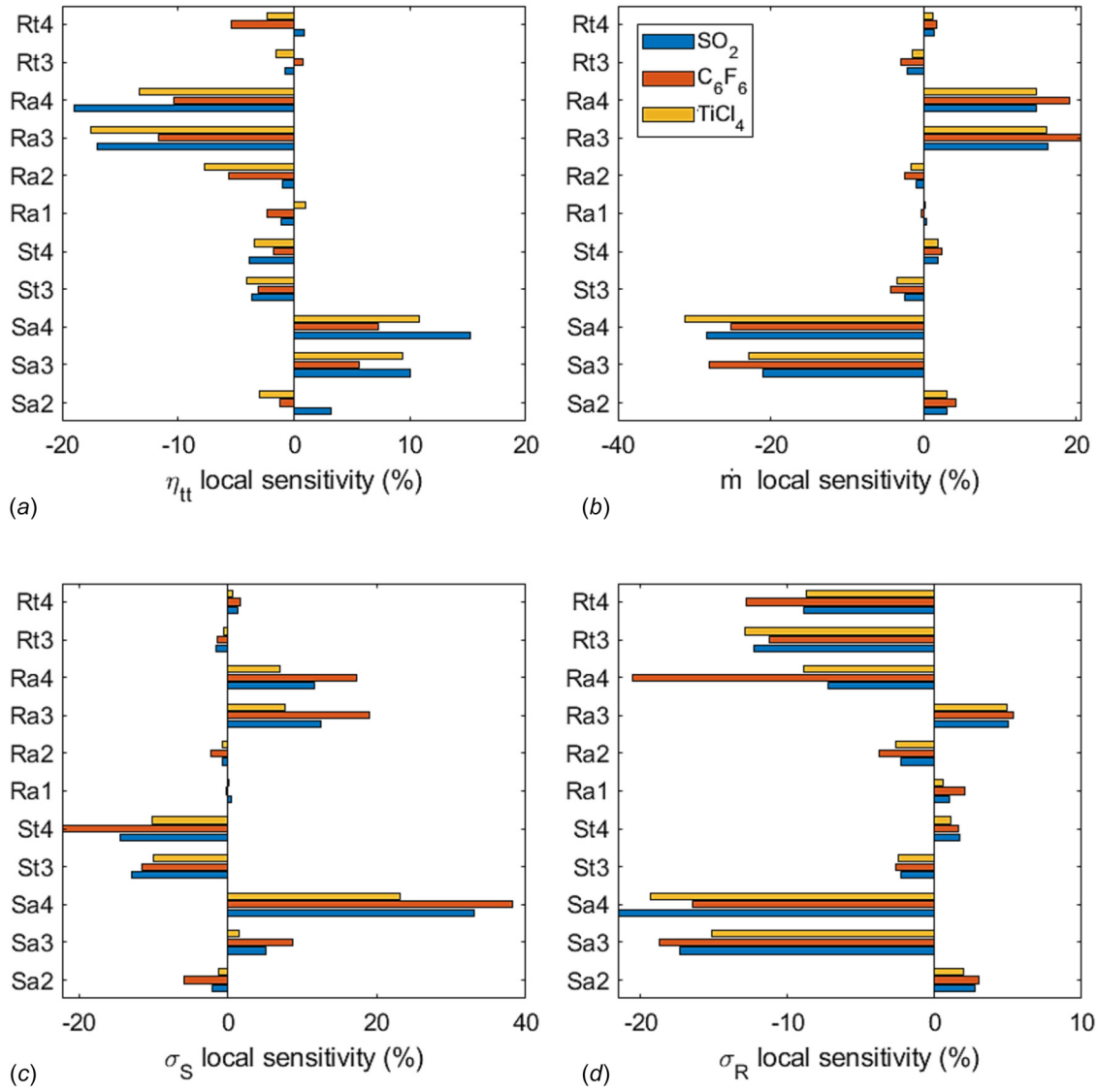

Fig. 13 Local sensitivity of objectives and constraints: (*a*) total-to-total efficiency, (*b*) mass flow rate, (*c*) stator maximum equivalent stress, and (*d*) rotor maximum equivalent stress

Table 9 Relative loss breakdown by component

	SO_2 reference	SO_2 optimum	C_6F_6 reference	C_6F_6 optimum	$TiCl_4$ reference	$TiCl_4$ optimum
Endwall	27.9%	22.2%	31.2%	20.5%	29.7%	17.6%
Profile	21.9%	23.8%	20.2%	23.9%	21.5%	20.1%
Trailing edge	15.4%	10.5%	13.5%	11.8%	13.7%	9.0%
Tip clearance	34.8%	43.5%	35.1%	43.8%	35.0%	53.3%

variation which could imply increasing the number of decision variables by a factor of two or three to obtain a full representation of a single blade. Thus, to make the optimization process more effective and accurate, particularly considering an extension to multiple stages, the number of decision variables should be limited to the most dominant variables. To this end, a sensitivity analysis has been performed to assess the importance of each input variable so that dominating parameters are established. The sensitivity of the output objectives and constraints to the 11 input variables used in this study is given in Fig. 13. The sensitivity of total-to-total efficiency is shown in Fig. 13(*a*) where the most dominant parameters are the stator and rotor blade angles near the trailing edge and the second midpoint on the angle distribution curve (point 3), as well as the outlet angles. Less dominant parameters affecting the efficiency, but non-negligible are the thickness points at the second half of the airfoil near the trailing edge (points 3 and 4). The other parameters also affect the efficiency; however, these are not significant. This indicates that the selected decision variables in this study are of reasonable importance, as anticipated during the initial selection process of variables. The local sensitivity of the mass-flow rate is shown in Fig. 13(*b*) where the dominant variables are mainly the blade angles within the second half of the airfoil (points 3 and 4). The stator and rotor blade angles at points 3 and 4 are also found to be important in determining the stator and rotor peak stresses. In addition, the local sensitivity of stator peak stress shown, as shown in Fig. 13(*c*), is affected by the thickness distribution parameters of the stator (St3 and St4) while the rotor peak stress, as shown in Fig. 13(*d*), is affected by the thickness distribution parameters of the rotor (Rt3 and Rt4).

5 Conclusion

The blade shape optimization of three turbine designs operating with CO_2 blended with $TiCl_4$, C_6F_6, or SO_2 has been presented. Comparing the reference and optimized blade geometries has revealed guidelines for improving the efficiency of the stage by reducing aerodynamic losses. The common adjustments are decreasing stator and rotor trailing edge thickness, increasing stator thickness near the trailing edge, decreasing rotor thickness near the trailing edge, and decreasing the rotor outlet angle.

The accuracy of the surrogate model has been improved by defining a number of refinement points alongside the initial learning points created using the design of experiments to improve the model accuracy. The optimized designs generated using the surrogate model have shown a deviation from the physical model in total-to-total efficiency of less than 0.3%, and a deviation in mass-flow rate and peak stresses of less than 1% in all the design cases.

The optimization results have shown an improvement in the aerodynamic performance of the three designs with efficiency increases of 2.54 pp, 2.06 pp, and 1.76 pp for the sCO_2–SO_2, sCO_2–C_6F_6, and sCO_2–$TiCl_4$ designs, respectively, while the mass-flow rate is kept within 2% of the design value and peak stresses are limited to 400 MPa. The results have shown that the optimized blades are achieved at a degree of reaction, flow coefficient, and loading coefficient around 0.63, 0.52, and 1.1, respectively, compared to design values of 0.5, 0.5, and 1.0, respectively. Assessing the loss breakdown reveals that the improved performance is mainly due to minimizing the endwall and profile losses for both the rotor and stator blades. However, the reduction in endwall losses is the most dominant.

Additionally, a sensitivity analysis has revealed that the design variables with the most significant impact on the total-to-total efficiency are the stator and rotor blade angles within the second part of the airfoil, which have also shown a significant effect on the mass-flow rate and peak stresses. The airfoil thickness near the trailing edge of the stator and the rotor dominate the stator and rotor peak stresses, respectively.

Ultimately, the results from this study have shown the validity of the approach taken by the authors in designing this type of turbine with novel working fluids, for which the available loss models are not tested or calibrated. In addition, it is found that the sensitivity of the aerodynamic and structural performance parameters to the blade thickness at and near the leading edge of both rotor and stator blades are low, and hence variables controlling these aspects could be omitted in future studies. The number of decision variables applied using the proposed methodology is recommended to be kept less than 11 in order for the surrogate model to accurately represent the physical CFD/FEA model, without requiring excessing computational power.

Funding Data

- European Union's Horizon 2020 (Funding Topic: LC-SC3-RES-11-2018, Grant Agreement No. 814985; Funder ID: 10.13039/100010661).

References

[1] Crespi, F., Sánchez, D., Martínez, G. S., Sánchez-Lencero, T., and Jiménez-Espadafor, F., 2020, "Potential of Supercritical Carbon Dioxide Power Cycles to Reduce the Levelised Cost of Electricity of Contemporary Concentrated Solar Power Plants," Appl. Sci., **10**(15), p. 5049.

[2] Crespi, F., Rodríguez De Arriba, P., Sánchez, D., Muñoz, A., and Sánchez, T., 2021, "The Potential of Supercritical Cycles Based on CO_2 Mixtures in Concentrated Solar Power Plants: An Exergy-Based Analysis," Proceedings of the Sixth International Seminar on ORC Power Systems, Virtual, Online, Munich, Germany, Oct. 11–13, pp. 11–13.

[3] White, M. T., Bianchi, G., Chai, L., Tassou, S. A., and Sayma, A. I., 2021, "Review of Supercritical CO_2 Technologies and Systems for Power Generation," Appl. Therm. Eng., **185**, p. 116447.

[4] Crespi, F., Rodríguez de Arriba, P., Sánchez, D., Ayub, A., Di Marcoberardino, G., Invernizzi, C. M., Martínez, G. S., Iora, P., Di Bona, D., Binotti, M., and Manzolini, G., 2022, "Thermal Efficiency Gains Enabled by Using CO_2 Mixtures in Supercritical Power Cycles," Energy, **238**, p. 121899.

[5] Morosini, E., Ayub, A., di Marcoberardino, G., Invernizzi, C. M., Iora, P., and Manzolini, G., Manzolini, G. J. E. C., and Management 2022, "Adoption of the $CO_2 + SO_2$ Mixture as Working Fluid for Transcritical Cycles: A Thermodynamic Assessment With Optimized Equation of State," Energy Convers. Manage., **255**, p. 115263.

[6] Cho, J., Choi, M., Baik, Y. J., Lee, G., Ra, H. S., Kim, B., and Kim, M., 2016, "Development of the Turbomachinery for the Supercritical Carbon Dioxide Power Cycle," Int. J. Energy Res., **40**(5), pp. 587–599.

[7] Zhang, H., Zhao, H., Deng, Q., and Feng, Z., 2015, "Aerothermodynamic Design and Numerical Investigation of Supercritical Carbon Dioxide Turbine," ASME Paper No. GT2015-42619.

[8] Crespi, F., Martínez, G., Rodriguez De Arriba, P., Sánchez, D., and Jiménez-Espadafor, F., 2021, "Influence of Working Fluid Composition on the Optimum Characteristics of Blended Supercritical Carbon Dioxide Cycles," ASME Paper No. GT2021-60293.

[9] Aqel, O., White, M., and Sayma, A., 2021, "Binary Interaction Parameter Uncertainty in the Optimisation of a Transcritical Cycle: Consequences on Cycle and Turbine Design," The 4th European sCO_2 Conference for Energy Systems, Online, Mar. 23–24.

[10] Brun, K., Friedman, P., and Dennis, R., 2017, *Fundamentals and Applications of Supercritical Carbon Dioxide (sCO2) Based Power Cycles*, Woodhead Publishing, Cambridge, UK.

[11] Sathish, S., Kumar, P., Namburi, A. N., Swami, L., Fuetterer, C., and Gopi, P. C., "Novel Approaches for sCO_2 Axial Turbine Design," ASME Paper No. GT2019-90606.

[12] Maral, H., Alpman, E., Kavurmacıoğlu, L., and Camci, C., 2019, "A Genetic Algorithm Based Aerothermal Optimization of Tip Carving for an Axial Turbine Blade," Int. J. Heat Mass Transfer, **143**, p. 118419.
[13] Berchiolli, M., Guarda, G., Walsh, G., and Pesyridis, A., 2019, "Turbocharger Axial Turbines for High Transient Response, Part 2: Genetic Algorithm Development for Axial Turbine Optimisation," Appl. Sci., **9**(13), p. 2679.
[14] Witanowski, Ł., Klonowicz, P., Lampart, P., Suchocki, T., Jędrzejewski, Ł., Zaniewski, D., and Klimaszewski, P., 2020, "Optimization of an Axial Turbine for a Small Scale ORC Waste Heat Recovery System," Energy, **205**, p. 118059.
[15] Persico, G., Romei, A., Dossena, V., and Gaetani, P., 2018, "Impact of Shape-Optimization on the Unsteady Aerodynamics and Performance of a Centrifugal Turbine for ORC Applications," Energy, **165**, pp. 2–11.
[16] Ennil, A. B., Al-Dadah, R., Mahmoud, S., Rahbar, K., and Aljubori, A., 2016, "Minimization of Loss in Small Scale Axial Air Turbine Using CFD Modeling and Evolutionary Algorithm Optimization," Appl. Therm. Eng., **102**, pp. 841–848.
[17] Asgarshamsi, A., Benisi, A. H., Assempour, A., and Pourfarzaneh, H., 2015, "Multi-Objective Optimization of Lean and Sweep Angles for Stator and Rotor Blades of an Axial Turbine," Proc. Inst. Mech. Eng., Part G J. Aerospace Eng., **229**(5), pp. 906–916.
[18] Noori Rahim Abadi, S. M. A., Ahmadpour, A., Abadi, S. M. N. R., and Meyer, J. P., 2017, "CFD-Based Shape Optimization of Steam Turbine Blade Cascade in Transonic Two Phase Flows," Appl. Therm. Eng., **112**, pp. 1575–1589.
[19] Kawatsu, K., Tani, N., Shimagaki, M., Uchiumi, M., Yamanishi, N., Mitsuhashi, K., and Mizuno, T., 2011, "Multi Objective Optimization of a Supersonic Axial Turbine Blade Row Shape for Rocket Engine Turbopump," AIAA Paper No. AIAA 2011-5784.
[20] Cho, S.-Y., Yoon, E.-S., and Choi, B.-S., 2002, "A Study on an Axial-Type 2-D Turbine Blade Shape for Reducing the Blade Profile Loss," KSME Int. J., **16**(8), pp. 1154–1164.
[21] Pakatchian, M. R., Saeidi, H., and Ziamolki, A., 2020, "CFD-Based Blade Shape Optimization of MGT-70 (3) Axial Flow Compressor," Int. J. Numer. Methods Heat Fluid Flow, **30**(6), pp. 3307–3321.
[22] Sivashanmugam, V. K., Arabnia, M., and Ghaly, W., 2010, "Aero-Structural Optimization of an Axial Turbine Stage in Three-Dimensional Flow," ASME Paper No. GT2010-23406.
[23] Schwerdt, L., Hauptmann, T., Kunin, A., Seume, J. R., Wallaschek, J., Wriggers, P., Panning-Von Scheidt, L., and Löhnert, S., 2017, "Aerodynamical and Structural Analysis of Operationally Used Turbine Blades," Procedia CIRP, **59**, pp. 77–82.
[24] Yoon, S., Vandeputte, T., Mistry, H., Ong, J., and Stein, A., 2016, "Loss Audit of a Turbine Stage," ASME J. Turbomach., **138**(5), p. 051004.
[25] De Servi, C. M., Burigana, M., Pini, M., and Colonna, P., 2019, "Design Method and Performance Prediction for Radial-Inflow Turbines of High-Temperature mini-Organic Rankine Cycle Power Systems," ASME J. Eng. Gas Turbines Power, **141**(9), p. 091021.
[26] Keep, J. A., and Jahn, I. H., 2019, "Numerical Loss Investigation of a Small Scale, Low Specific Speed Supercritical CO_2 Radial Inflow Turbine," ASME J. Eng. Gas Turbines Power, **141**(9), p. 091003.
[27] Salah, S. I., Khader, M. A., White, M. T., and Sayma, A. I., 2020, "Mean-Line Design of a Supercritical CO_2 Micro Axial Turbine," Appl. Sci., **10**(15), p. 5069.
[28] Binotti, M., Marcoberardino, G. D., Iora, P., Invernizzi, C., and Manzolini, G., 2020, "SCARABEUS: Supercritical Carbon Dioxide/Alternative Fluid Blends for Efficiency Upgrade of Solar Power Plants," AIP Conference Proceedings, **2303**(1), p. 130002.
[29] Aungier, R. H., 2006, *Turbine Aerodynamics*, ASME, New York.
[30] Abdeldayem, A., White, M. T., and Sayma, A. I., 2021, "Comparison of CFD Predictions of Supercritical Carbon Dioxide Axial Flow Turbines Using a Number of Turbulence Models," ASME Paper No. GT2021-58883.
[31] Jang, H. J., Kang, S. Y., Lee, J. J., Kim, T. S., and Park, S. J., 2015, "Performance Analysis of a Multi-Stage Ultra-Supercritical Steam Turbine Using Computational Fluid Dynamics," Appl. Therm. Eng., **87**, pp. 352–361.
[32] Touil, K., and Ghenaiet, A., 2019, "Simulation and Analysis of Vane-Blade Interaction in a Two-Stage High-Pressure Axial Turbine," Energy, **172**, pp. 1291–1311.
[33] Dubiez-Le Goff, S., Couturier, R., Guétaz, L., and Burlet, H., 2004, "Effect of the Microstructure on the Creep Behavior of PM Udimet 720 Superalloy—Experiments and Modeling," Mater. Sci. Eng.: A, **387–389**, pp. 599–603.
[34] Hatami, M., Cuijpers, M. C., and Boot, M. D., 2015, "Experimental Optimization of the Vanes Geometry for a Variable Geometry Turbocharger (VGT) Using a Design of Experiment (DoE) Approach," Energy Convers. Manage., **106**, pp. 1057–1070.
[35] Toft, H. S., Svenningsen, L., Moser, W., Sørensen, J. D., and Thøgersen, M. L., 2016, "Assessment of Wind Turbine Structural Integrity Using Response Surface Methodology," Eng. Struct., **106**, pp. 471–483.
[36] Wang, S., Jian, G., Xiao, J., Wen, J., and Zhang, Z., 2017, "Optimization Investigation on Configuration Parameters of Spiral-Wound Heat Exchanger Using Genetic Aggregation Response Surface and Multi-Objective Genetic Algorithm," Appl. Therm. Eng., **119**, pp. 603–609.
[37] Viana, F. A., Haftka, R. T., and Steffen, V., 2009, "Multiple Surrogates: How Cross-Validation Errors Can Help us to Obtain the Best Predictor," Struct. Multidiscip. Optim., **39**(4), pp. 439–457.
[38] Scrzenie, F., and Maurer, G., 1984, "Development of Udimet 720 for High Strength Disk Application," Superalloys, pp. 573–580.
[39] Denton, J. D., 1993, "Loss Mechanisms in Turbomachines," ASME Paper No. 93-GT-435.
[40] Xiao, X., Mccarter, A. A., and Lakshminarayana, B., 2001, "Tip Clearance Effects in a Turbine Rotor: Part I—Pressure Field and Loss," ASME J. Turbomach., **123**(2), pp. 296–304.